

3D Porous Biomass Derived Carbon Composite Modified with (Ni,Co)Se Particles for High-Performance Supercapacitors

Jiaquan Liu,^[a] Zitong Ding,^[a] Qiuman Zhou,^[a] Lanfei Wei,^[a] and Yurong Yan^{*[a, b]}

Modification with transition metal compounds is an effective strategy to improve the capacitance of biomass derived carbon. In this work, high-performance (Ni,Co)Se/banana leaves derived carbon ((Ni,Co)Se/BLC) composite with 3D porous structure was prepared by two-step carbonization and subsequent hydrothermal reaction process. The prepared (Ni,Co)Se/BLC exhibits a high specific capacitance of 840.6 F/g at a current density of 1 A/g, which is more than five times comparing with the carbon matrix. Asymmetric supercapacitor, assembled with the

(Ni,Co)Se/BLC composite as the positive electrode and BLC as the negative electrode, exhibits a wide potential window of 1.5 V, delivers a high energy density of 34.3 Wh/kg at a power density of 749.8 W/kg, and the power density can reach 7500 W/kg at the energy density of 19.4 Wh/kg. The results reveal that the modification of metal selenide can greatly improve the electrochemical properties of biomass derived carbon, which is significant for the application of biowaste in supercapacitor electrode materials.

Introduction

In the past century, the development of industrial has consumed large amounts of fossil fuels, triggering global climate and energy crisis.^[1,2] The promotion of renewable sources of energy such as solar, wind and tide is bringing a new era of sustainable development.^[3-5] At the same time, it requires more efficient and stable energy storage devices.^[6] Supercapacitors, with many unique properties such as rapid charging/discharging ability, long cycle life and outstanding power density have attracted more and more attention.^[7,8]

Because of its outstanding structural stability and flexible surface modification, carbon and its composites are widely studied as electrode materials for supercapacitors.^[9] However, carbon based materials such as carbon fibers,^[10,11] graphene^[12] or MOF-derived activated carbon^[13,14] are all expensive and essentially derived from fossil sources.^[15] Therefore, researchers changed their attention to the vast quantities of biowaste that is renewable and widely available. Through simple activation and carbonization, the massive waste can be converted into activated carbon with high specific surface area to maximize the utilization of the resources.^[16] Banana is one of the oldest cultivated fruits in the world, widely grown in about 130 countries in tropical and subtropical regions. According to Food and Agriculture Organization of the United Nations (FAO), the

global production of bananas in 2020 was over 120 million tons (<http://www.fao.org>). It produces a lot of fallen leaves as the bananas grow, especially since they only bear fruit once in their life, the entire tree will be cut down after harvest, resulting in a large amount of waste mainly consisting of stems and leaves. It is of great ecological and economic significance to explore more utilization way of banana leaves. The main components of banana leaves are organics such as cellulose, hemicellulose and lignin, which are all suitable carbon sources.^[17] In addition, banana leaves contain a variety of metal ions, such as sodium (Na), potassium (K) and calcium (Ca), etc., which can be released after KOH activation, and form a hierarchical pore structure that facilitates ion transport.^[18] With banana leaves as precursor, Apriwandi et al.^[19] prepared an activated carbon through chemical activation and physical activation, which possessed a specific surface area of 623 m²/g and exhibited excellent electrochemical properties. Roy et al.^[18] prepared a banana leaves derived carbon with K₂CO₃ as activator, and assembled a symmetric supercapacitor with ionic liquid as electrolyte, showing a specific capacitance of 190 F/g. However, carbon materials usually store charges through the electrochemical double-layer formed between electrode and electrolyte, the specific capacitance depends on the limited contact area. The unmodified pure biomass derived activated carbon only shows a limited specific capacitance less than 300 F/g.^[20]

The effective strategy to improve the limited specific capacitance of biomass derived carbon is to modify conductive polymers or transition metal compounds that can provide pseudo-capacitance on their surface.^[5] Transition metal oxides (such as MnO₂,^[21] Mn₂O₃,^[22] Co₃O₄,^[23] Fe₂O₃,^[24-26] TiO₂,^[27]) are the most common pseudo-capacitor materials in previous researches.^[4,28] Vijayan et al.^[22] coated Mn₂O₃ on the palm shell-derived activated carbon (Mn₂O₃@AC) using one-step activation-coating procedure. The assembled supercapacitor showed more than twice specific capacitance than that of pure carbon.

[a] J. Liu, Z. Ding, Q. Zhou, L. Wei, Prof. Y. Yan
School of Materials Science and Engineering
South China University of Technology
Wushan, Guangzhou (P. R. China)
E-mail: yryan@scut.edu.cn

[b] Prof. Y. Yan
Key Lab of Guangdong High Property & Functional Polymer Materials
Wushan, Guangzhou (P. R. China)

 Supporting information for this article is available on the WWW under
<https://doi.org/10.1002/batt.202300362>

Yu et al.^[24] prepared a composite by aligning α -Fe₂O₃ nanorods on the wheat flour derived porous carbon skeleton. The electrode exhibited a specific capacitance of 706 F/g in 1 M Li₂SO₄ electrolyte. However, compared with metal oxides, transition metal selenides have higher theoretical charge storage capacity and abundant crystal structure,^[29] and have been proved to show excellent properties as electrode materials. Nickel-based (NiSe,^[30] NiSe₂,^[31,32] Ni₃Se₂,^[33] etc.) and cobalt-based selenides (CoSe₂,^[29] CoSe,^[34] Co_{0.85}Se,^[35] Co₉Se₈,^[32] etc.) are the two most widely studied in previous research. Furthermore, the bimetallic compounds of Ni and Co have better properties than the corresponding single-phase compounds^[36,37] because of the combination of the high capacitance of nickel-based materials and the excellent stability of cobalt-based materials.

In this work, we successfully loaded highly conductive metal selenides onto banana leaves derived porous carbon (BLC) to achieve a large increase in specific capacitance. Banana leaves (BL) were used as precursors to prepare biomass derived carbon with hierarchical porous structure through KOH activation and the prepared BLC has a high specific surface area of 1068 m²/g. (Ni,Co)Se nanospheres were synthesized by hydrothermal method on the biomass derived carbon where porous structure provided sufficient growth sites for the nanospheres. (Ni,Co)Se/BLC composite exhibits a specific capacitance of 840.6 F/g at a current density of 1 A/g. The asymmetric supercapacitor assembled with BLC as the negative electrode shows the highest energy density of 34.3 Wh/kg at a power density of 749.8 W/kg.

Results and Discussion

The schematic illustration of the preparation of BLC and (Ni,Co)Se/BLC composite was depicted in Figure 1. Firstly, banana leaves derived activated carbon with hierarchical porous structure was obtained by two-step carbonization. Using this activated carbon as matrix, (Ni,Co)Se was loaded by subsequent hydrothermal reaction. The prepared samples were denoted as (Ni,Co)Se-*n*/BLC, where '*n*' indicates different loading amount. The electrochemical performance of activated carbon used for supercapacitor is affected by its specific surface area, pore size distribution and surface active groups, which are

related to the activation method and activation parameter such as time and temperature.^[1] Chemical activation with KOH as activator is the most widely used method for preparing biomass derived carbon due to its convenient operation, controllable condition and high specific surface area of product.^[4,15] It is crucial to adjust the ratio of carbon precursor and activator during the chemical activation, which will affect the pore structure of the final prepared active carbon, and further affect the growth of metal compounds. Samples with different KOH ratios were prepared and the SEM images were showed in Figure 2. Compared with the smooth structure of the non-activated sample (Figure 2a), samples treated with KOH present hierarchical porous microstructure. The three-dimensional interconnected porous framework constructed by macropores, mesopores and micropores promises a large specific surface area that facilitates the penetration of electrolyte, and provides abundant storage space and fast diffusion channels for ions, therefore reduces the charge transfer resistance.^[38] As showed in Figure 2(b and c), more KOH will promote the formation of pores. However, too much KOH is adverse to the formation of micropores, and even causes the collapse of the porous structure,^[9,39] as showed in Figure 2(e). It can be observed that BLC1.5 has a relatively complete hierarchical interconnected porous structure among these samples. Subsequent electrochemical measurements also verify that it shows the best electrochemical performance.

The microstructure of the samples after hydrothermal reaction is shown in Figure 3, indicating that (Ni,Co)Se nanospheres were successfully loaded onto porous activated carbon. The nanospheres with uniform diameters of nearly 500 nm are evenly distributed on the surface of BLC and even the inner wall of the pores. The rough popcorn-like surface of the nanospheres provides a large number of active sites for redox reactions. In addition, some smaller (50–100 nm) nanosheets are found uniformly embedded on the carbon wall, which are considered to be the initial form of the (Ni,Co)Se nanospheres. As showed in Figure 3(a), few (Ni,Co)Se nanospheres are found in (Ni,Co)Se-0.5/BLC, which only provides little contribution to capacitance improvement. However, too many nanospheres in (Ni,Co)Se-1.5/BLC will aggregate on the carbon matrix, as showed in Figure 3(d), which is not conducive to the sufficient contact with electrolyte. Besides, too many nanospheres will



Figure 1. Schematic illustration of the synthetic process for BLC and (Ni,Co)Se/BLC composite.

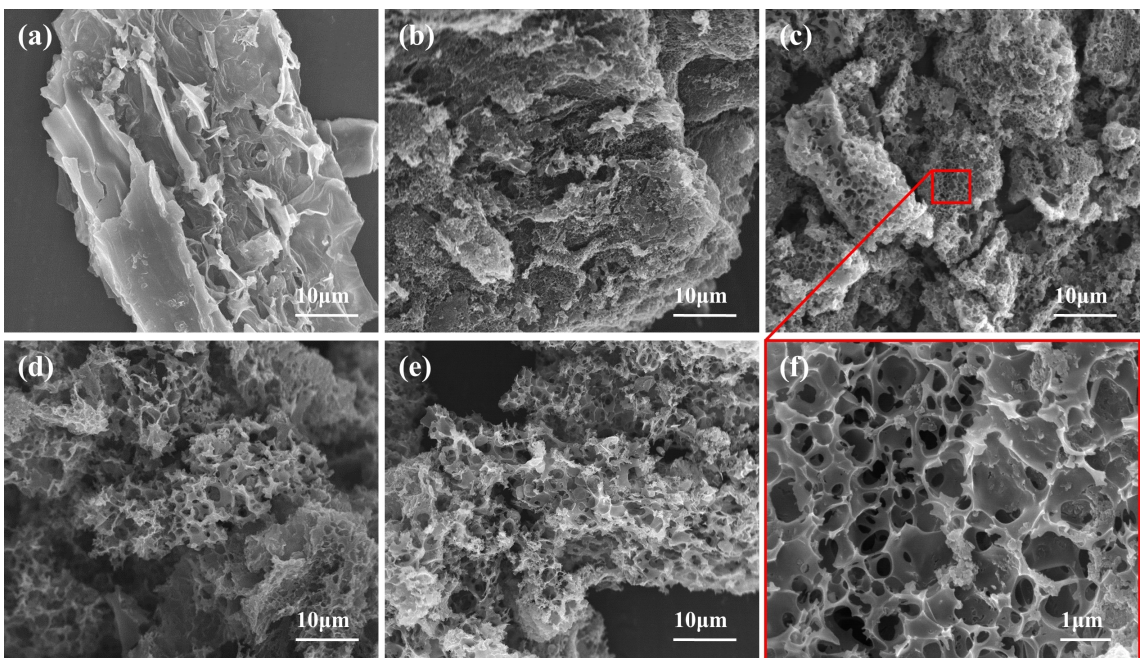


Figure 2. SEM images of the biomass derived carbon with different KOH ratio of a) 1:0 (without KOH), b) 1:1, c) 1:1.5, d) 1:2, and e) 1:2.5, respectively, f) partial enlarged image of (c).

almost completely cover up the original porous structure of active carbon and hinder the transport of iron, resulting in a decline in electrochemical performance. It can be observed from Figure 3(c) that (Ni,Co)Se-1.0/BLC achieves a great balance between the pseudo-capacitance and the specific surface area. The content of elements in the samples with different (Ni,Co)Se loads was shown in Table S2, which verifies that the proportion of the carbon matrix decreases from 60.67% to 37.04% with the increase of (Ni,Co)Se. The content of each element is basically consistent with the theoretical value, which also indicates the high efficiency of the hydrothermal reaction. The TEM image (Figure 3e) verifies that the nanospheres are evenly distributed. Besides, the elemental mapping images of Ni, Co and Se in Figure 3(f) are highly coincident, which suggests the successful synthesis of (Ni,Co)Se. Lattice fringes can be clearly observed in Figure 3(g), where the fringes of 0.272 nm and 0.262 nm correspond to the crystal planes of $\text{Ni}_{0.85}\text{Se}$ (101) and Co_9Se_8 (400), respectively.

The crystal structures of the samples were characterized by powder X-ray diffraction (XRD) technique. Just like most biomass derived carbons, there are two typical broad peaks at 2θ of $\sim 25^\circ$ and $\sim 43^\circ$ (Figure 4a) which are ascribed to the (002) and (110) crystal planes of graphite, indicating the amorphous structure of the active carbon.^[39,40] The diffraction peaks of (Ni,Co)Se/BLC at 2θ of 33.152°, 44.949° and 50.493° correspond to the (101), (102) and (110) crystal planes of $\text{Ni}_{0.85}\text{Se}$ (JCPDS NO. 18-0888), respectively. The peaks at 2θ of 28.217°, 29.655°, 45.138°, 49.382° and 58.559° are indexed to the (311), (222), (511), (440) and (622) planes of Co_9Se_8 (JCPDS NO. 09-0233). Diffraction patterns of all the samples contain the diffraction peaks of $\text{Ni}_{0.85}\text{Se}$ and Co_9Se_8 (Figure S3), indicating the successful synthesis of the (Ni,Co)Se/BLC composite. Raman

spectrum was also employed to characterize the graphitization degree of activated carbon, as showed in Figure 4(b). The D-band (1340 cm^{-1}) is corresponded to the structural disorder and the G-band (1580 cm^{-1}) is related to the ordered graphite layers. The relative intensity ratio (I_D/I_G) of D- to G-bands reflects the proportion of graphitic defects in the activated carbon.^[41] It can be observed that the I_D/I_G ratio of activated carbon increases after KOH activation, indicating the improved surface defects of the material, which is beneficial to the improvement of the specific surface area.^[39] It can also provide more active sites for the subsequent hydrothermal reaction,^[38] which is conducive to the load of metal selenides and the improvement of the capacitance.

With (Ni,Co)Se-1.0/BLC as the representative, X-ray photo-electron spectroscopy (XPS) was employed to further confirm the composition of the as-prepared material. Full spectrum (Figure 4c) demonstrates that the sample is composed of C, Ni, Co, Se, O and Si, where the small amount of Si comes from biomass (Figure S5).^[21] The O element is from the oxygen-containing functional groups of BLC^[38,39] and unavoidable surface oxidation.^[37] Figure 4(d-f) shows the high-resolution emission spectra of Ni 2p, Co 2p and Se 3d. For the Ni 2p spectrum, the peaks positioned at 871.89 eV and 854.06 eV are in accordance with the Ni^{2+} . The $\text{Ni} 2p_{1/2}$ and $\text{Ni} 2p_{3/2}$ peaks at 879.85 eV and 861.69 eV are corresponding to Ni^{3+} , accompanied by two satellite peaks (Sat.).^[42-44] As the spectrum of Co 2p showed, there are also two different chemical valence states of Co in the composite, where the peaks situated at 781.99 eV for $\text{Co} 2p_{1/2}$ and 797.73 eV for $\text{Co} 2p_{3/2}$ can be assigned to Co^{2+} , and the peaks at 780.45 eV and 795.14 eV are originate from Co^{3+} . The satellites peak of Co 2p (Sat.) can also be observed at 786.93 eV and 797.73 eV.^[45,46] Furthermore, the peak in the

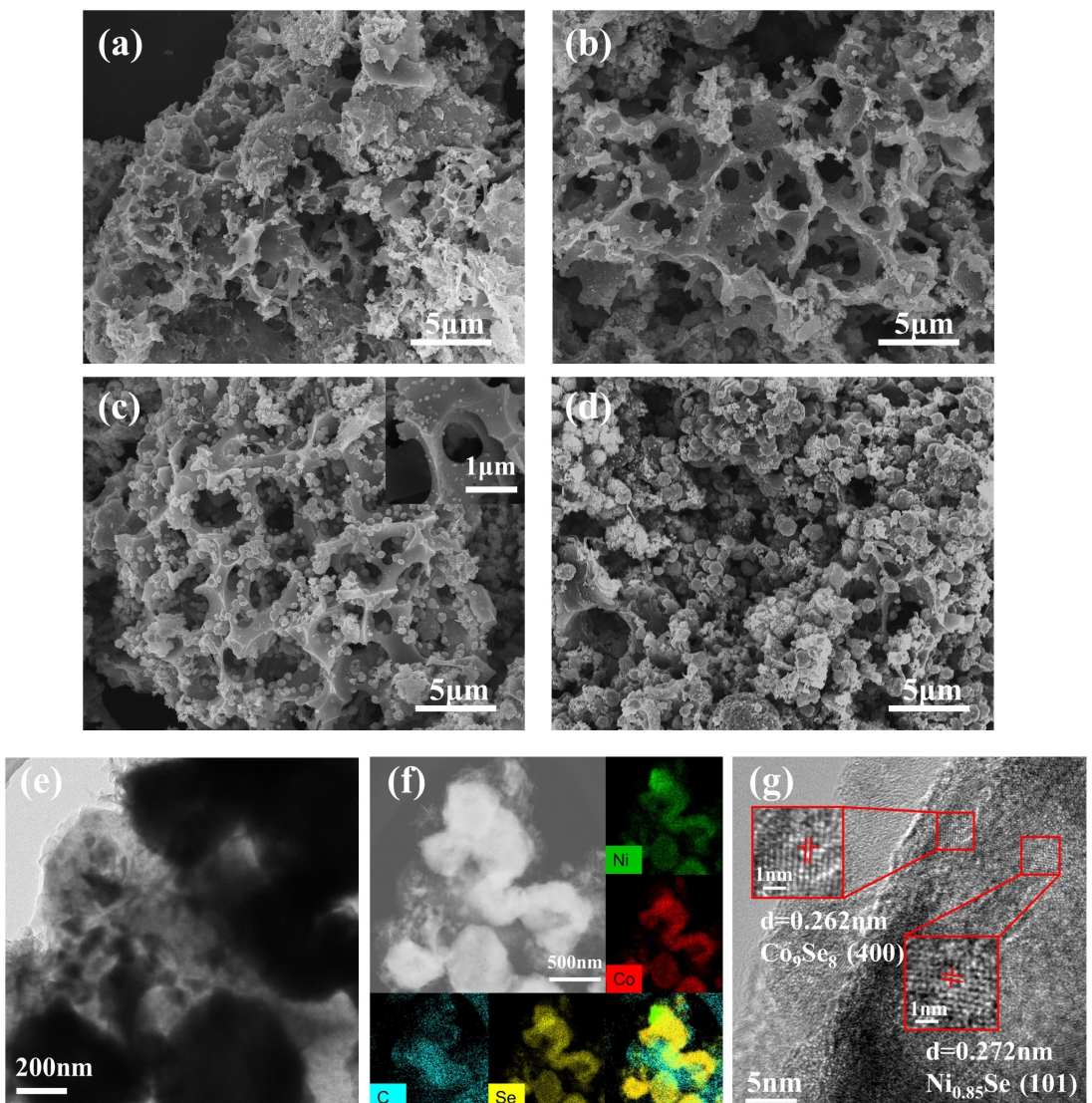


Figure 3. SEM images of the composites a) (Ni,CoSe-0.5/BLC, b) (Ni,CoSe-0.75/BLC, c) (Ni,CoSe-1.0/BLC, d) (Ni,CoSe-1.5/BLC and e) TEM image, f) elemental mapping images, g) HRTEM of (Ni,CoSe-1.0/BLC)

Se 3d spectrum at 54.73 eV is the typical feature of metal-selenium bonds, and the peak at 59.46 eV is from the surface oxidation state of Se.^[36,47] The above analysis is highly consistent with XRD data, demonstrating the successful preparation of the composites.

The porosity of the prepared samples was further analyzed by N₂ adsorption-desorption technology. Figure 4(g) shows the N₂ adsorption-desorption isotherms of BLC1.5 and (Ni,CoSe-1.0/BLC, where both present I/V-type isotherm characteristics with a sharp adsorption inflection at low relative pressure and a hysteresis loop at moderate relative pressure, indicating the micro-mesoporous structure.^[40,41,48] As listed in Table 1, BLC1.5 exhibits a high SSA up to 1068 m²/g and a satisfactory pore volume of 0.62 cm³/g, in which the volume of micropore accounts for 55%. However, all these values are greatly reduced when the metal selenide is loaded to form the composite. It can be explained that, on the one hand, metal selenide shows

Table 1. Pore textural properties of BLC1.5 and (Ni,CoSe-1.0/BLC.

Sample	S _{BET} [m ² /g]	S _{micro} [m ² /g]	V _{total} [cm ³ /g]	V _{micro} [cm ³ /g]
BLC1.5	1068	826	0.62	0.34
(Ni,CoSe-1.0/BLC	184	143	0.15	0.06

much higher density than activated carbon, which will reduce the specific surface area and pore volume; on the other hand, pore structures may be destroyed in the process of hydrothermal reaction especially the micropore, resulting in a decrease of the ratio of micropore volume to total volume. In addition, the loading of metal selenides may clog some of the pores, also causing a decrease in the specific surface area. The pore size distributions of BLC1.5 and (Ni,CoSe-1.0/BLC are illustrated in Figure 4(h), where the curve of (Ni,CoSe-1.0/BLC composite is similar to that of BLC1.5. The pore sizes of the

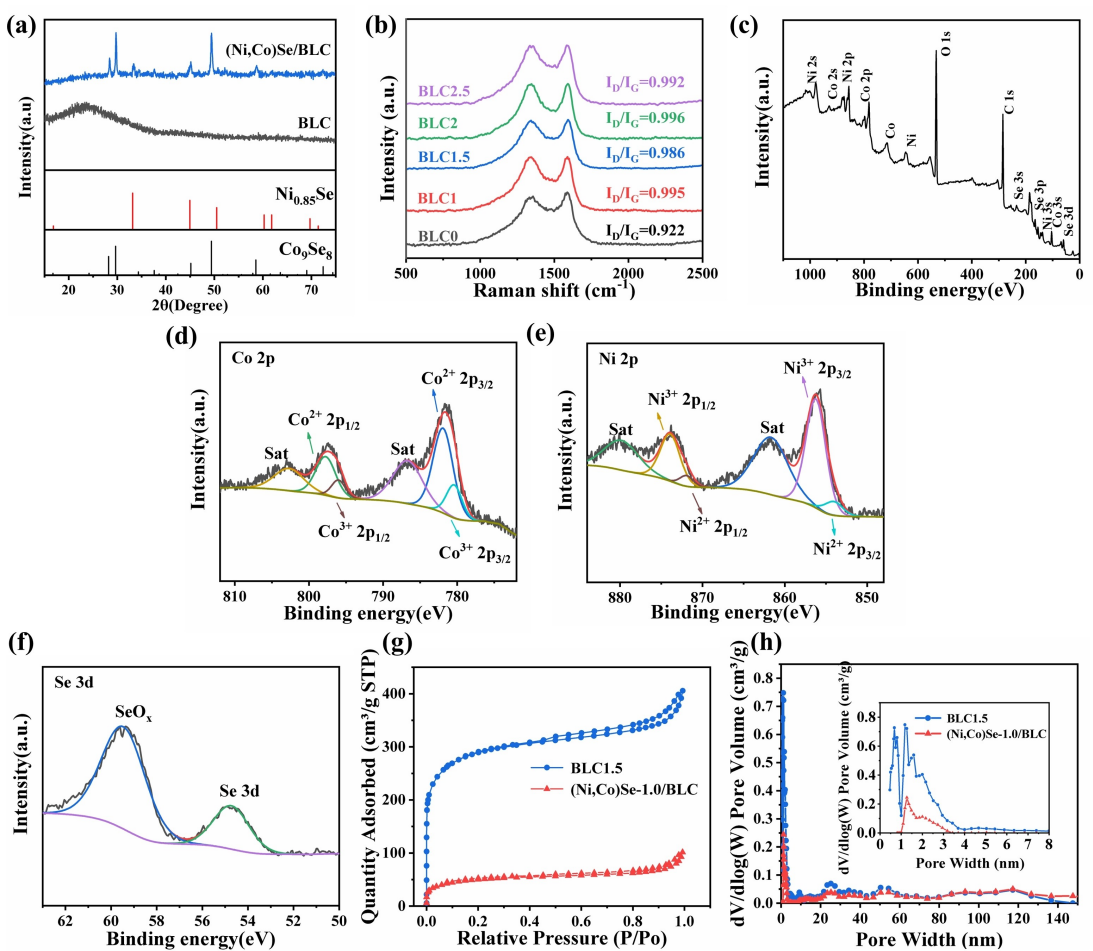


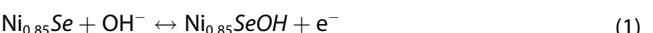
Figure 4. a) XRD patterns of BLC and (Ni,Co)Se/BLC composite. b) Raman spectrums of BLC with different KOH ratio. c) Full XPS spectrum and high-resolution emission spectra of d) Co 2p, e) Ni 2p and f) Se 3d of (Ni,Co)Se-1.0/BLC. g) N_2 adsorption and desorption isotherms and h) pore size distribution of BLC1.5 and (Ni,Co)Se-1.0/BLC composite.

micropore in BLC1.5 are mainly concentrated at 0.5–1.0 nm and 1–2 nm, while only the latter is retained after the hydrothermal reaction. In addition, mesoporous pores with sizes concentrated at 20–40 nm and a small amount of macropores larger than 50 nm can also be observed in both BLC1.5 and (Ni,Co)Se-1.0/BLC. The result of N_2 adsorption-desorption technology confirms that the composite retains the hierarchical porous structure of the biomass derived carbon matrix, which provides a channel for fast ion transport and promotes the accessibility of the electrolyte.

The electrochemistry performances of the samples were investigated in a three-electrode system using 3 M KOH aqueous as the electrolyte. Figure 5(a) shows the cyclic voltammetry (CV) cures of BLCn which all present typical quasi-rectangular shape at 100 mV/s, indicating the double-layered capacitive behavior.^[49,50] BLC1.5 has the largest integrated area of CV curve, suggesting the highest specific capacitance in the prepared activated carbons, which can be further confirmed by the GCD cures. The specific capacitances calculated according to the GCD curves of BLC0, BLC1, BLC1.5, BLC2 and BLC2.5 are 109.3, 129.5, 158.7, 136.5 and 114.3 F/g, respectively, which is consistent with the inference of SEM images. As showed in

Figure 5(d), CV curve of BLC1.5 maintains a quasi-rectangular shape when the scan rate increases to 150 mV/s. The specific capacitance of BLC1.5 at different current densities can be calculated from Figure 5(e), where the curves maintain the triangular shape as the current density changed, suggesting a typical EDLC behavior.^[39] As showed in Figure 5(f), the capacitance retention of BLC1.5 could be as high as 74.9% at 15 A/g.

Figure 6(a) shows the CV curves of the composites with different metal selenide loading qualities at 10 mV/s. It can be observed that all the curves show a pair of symmetric redox peaks, indicating the pseudo-capacitor behavior.^[34] The charge storage mechanism is based on the rapid reversible redox reaction on the surface of the material, which can be described by the following equations:^[36,47]



The GCD curves of the samples at the current density of 1 A/g are showed in Figure 6(b). Unlike the symmetrical triangular curves of BLC, there is a pair of visible potential

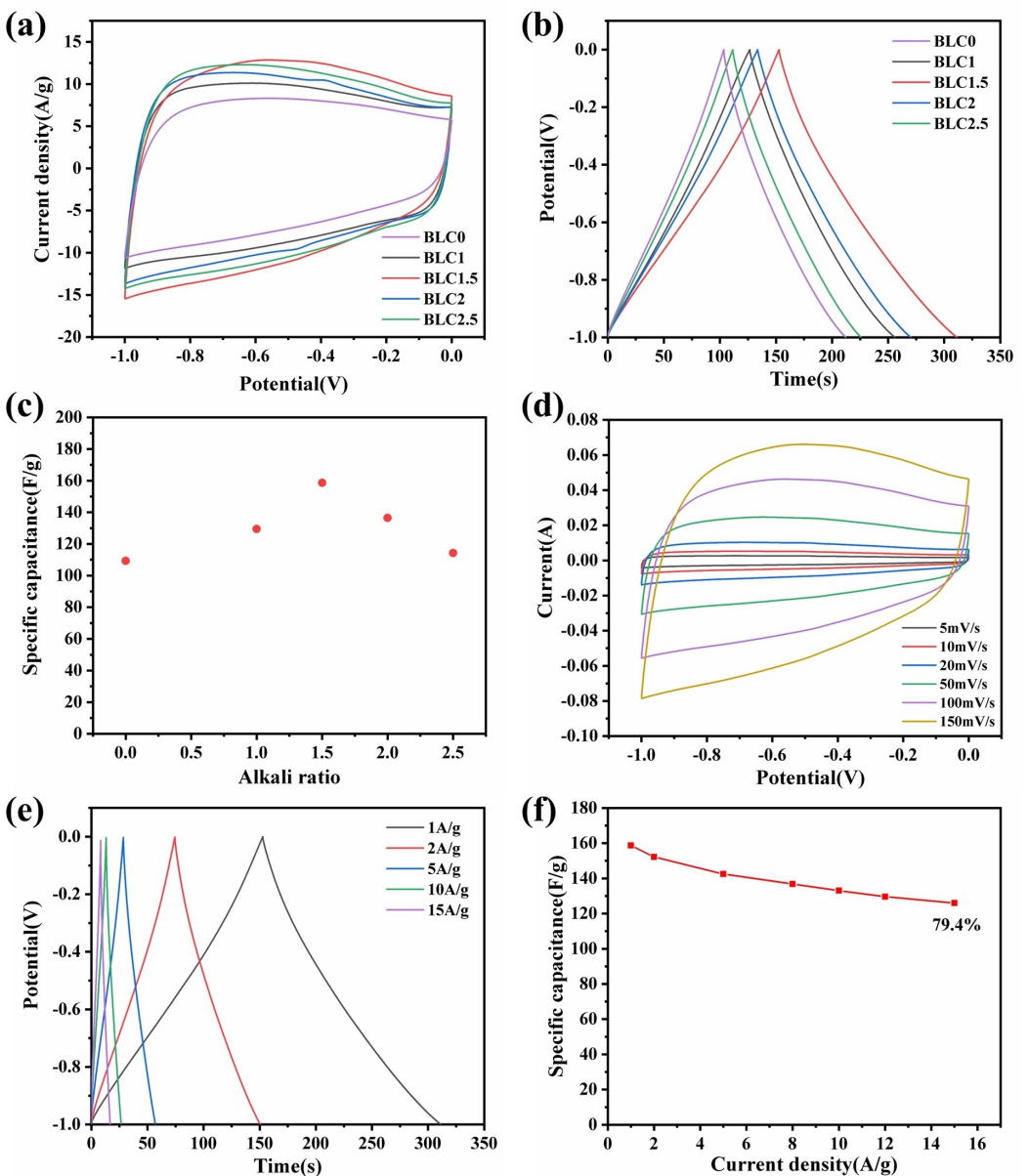


Figure 5. a) CV curves of BLC_n at scan rate of 100 mV/s. b) GCD curves of BLC_n at current density of 1 A/g. c) Specific capacitance of BLC with different alkali ratio at 1 A/g. d) CV curves of BLC1.5 at different scant rates. e) GCD curves of BLC1.5 at different current densities. f) Specific capacitances of BLC1.5 at different current densities

plateaus in all cures owing to the reversible redox reaction during the charge/discharge processes.^[47] It is obvious that (Ni,Co)Se-1.0/BLC has the longest charge-discharge time, suggesting the best charge storage performance. The specific capacitances of (Ni,Co)Se-0.5/BLC, (Ni,Co)Se-0.75/BLC, (Ni,Co)Se-1.0/BLC and (Ni,Co)Se-1.5/BLC are 306.8, 373.8, 840.6 and 461.0 F/g, respectively, which are much higher than BLC. Particularly, the specific capacitance of (Ni,Co)Se-1.0/BLC is even 5 times higher than that of the original activated carbon matrix under the same condition. The improvement in specific capacitance is attributed to the contribution of pseudo-capacitance provided by Ni–Co selenides. The specific capacitance increases with the rise of the loading amount in a certain

range, while too much metal selenide will accumulate on the surface of activated carbon, which will decrease the contact with the electrolyte. (Ni,Co)Se-1.0/BLC also shows higher specific capacitance than pure (Ni,Co)Se (513.2 F/g). This is because activated carbon provides a larger surface area and promotes the uniform distribution of the selenides, preventing them from aggregating and increasing the contact area with the electrolyte. Figure 6(c) shows the CV curves of (Ni,Co)Se-1.0/BLC at different scan rates from 5 to 100 mV/s. The redox peak changes with increasing of the scan rate due to the change of the charge diffusion polarization within the material.^[36] Figure 6(d) is the GCD curves of (Ni,Co)Se-1.0/BLC at different current densities from 1 to 10 A/g. All the cures maintain a

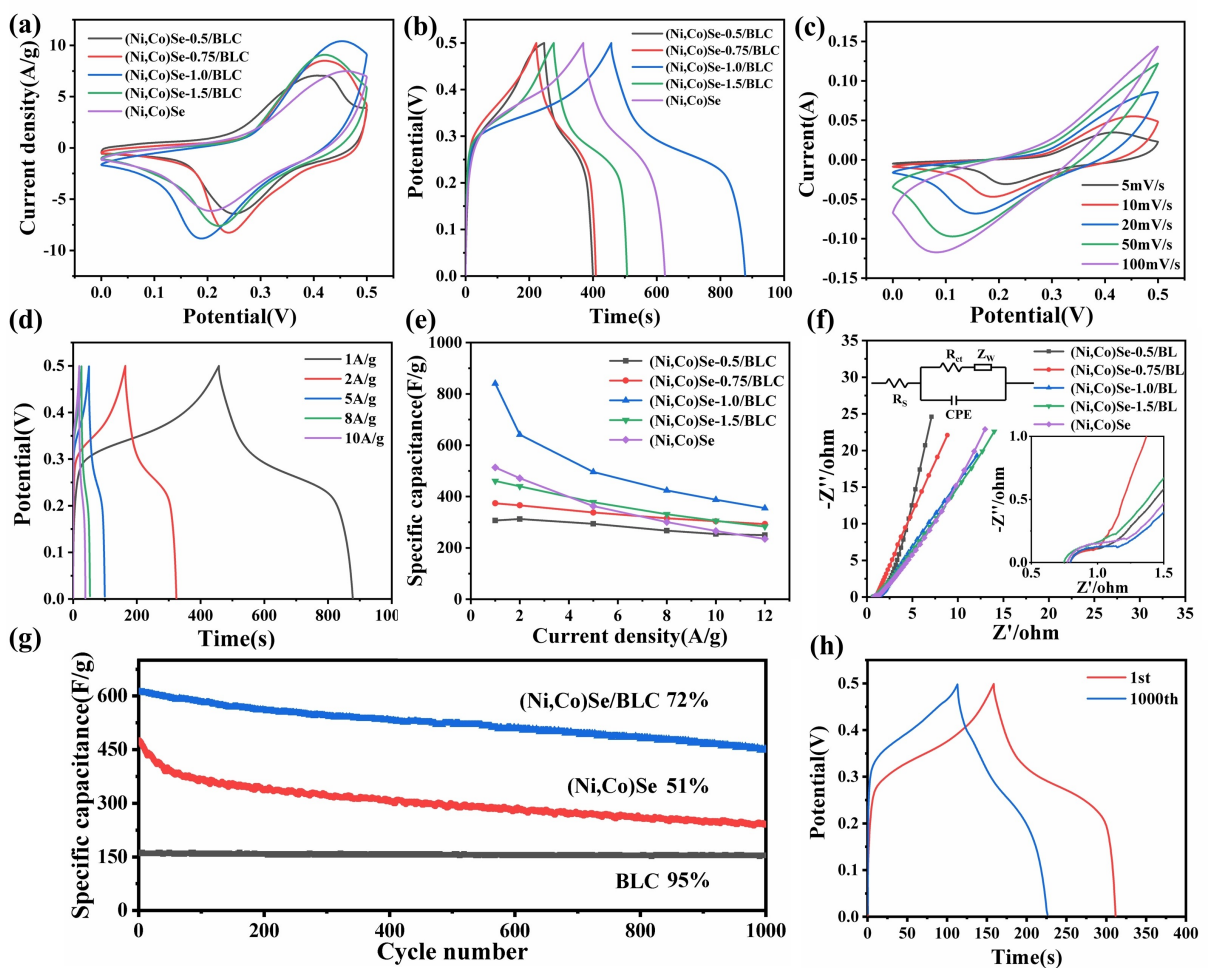


Figure 6. a) CV curves of (Ni,Co)Se/BLC and (Ni,Co)Se at scan rate of 10 mV/s. b) GCD curves of (Ni,Co)Se/BLC and (Ni,Co)Se at current density of 1 A/g. c) CV curves of (Ni,Co)Se-1.0/BLC at different scant rates. d) GCD curves of (Ni,Co)Se-1.0/BLC at different current densities. e) Specific capacitances of (Ni,Co)Se/BLC and (Ni,Co)Se at different current densities. f) Nyquist plots of (Ni,Co)Se/BLC and (Ni,Co)Se. g) Cycling stability of BLC1.5 and (Ni,Co)Se-1.0/BLC. h) Comparison of GCD curves of (Ni,Co)Se-1.0/BLC before and after cycling.

relatively symmetric shape, suggesting the ideal reversibility of the redox reaction. It is visible in Figure 6(e) that (Ni,Co)Se-1.0/BLC always holds the highest specific capacitances among the samples although the specific capacitances decrease with the increase of current density. The specific capacitance of (Ni,Co)Se-1.0/BLC remains 355.2 F/g even at a current density of 12 A/g. When the current density increases from 5 A/g to 12 A/g, the specific capacitance retention of (Ni,Co)Se is significantly lower than that of the composite material. At lower current density (1 and 2 A/g), the electrolyte ions move slowly and the pure (Ni,Co)Se exhibits a specific capacitance second only to (Ni,Co)Se-1.0/BLC. However, the low porosity and low specific surface area of (Ni,Co)Se limit the rapid movement of the electrolyte ions at high current density, so that at a current density of 12 A/g, the specific capacitance of (Ni,Co)Se is lower than that of other samples.

Furthermore, as shown in the supporting information, the single-metal selenide composites NiSe-1.0/BLC and CoSe-1.0/BLC were synthesized and characterized in the same way. The electrochemical performance is shown in Figure S6. At a current

density of 1 A/g, the specific capacitance of CoSe-1.0/BLC and NiSe-1.0/BLC is 122.8 and 310 F/g, respectively, which is far lower than that of (Ni,Co)Se-1.0/BLC. When the current density increases to 10 A/g, the capacitance retention rates of CoSe-1.0/BLC, NiSe-1.0/BLC and (Ni,Co)Se-1.0/BLC are 66.8%, 35.5% and 46.1%, respectively. Compared with the poor capacitance retention of Ni-based composite and low specific capacitance of Co-based composite, the integration of Ni and Co atoms makes the material show better properties than that of single-phase composites.^[36]

Table 2 lists the capacitance comparisons of as-prepared (Ni,Co)Se-1.0/BLC in this work with the reported metal compounds/biomass derived carbon composites. It is showed that the biomass-based composite synthesized in this work represents higher specific capacitance than the reported materials.

Electrochemical impedance spectroscopy (EIS) was also used to evaluate the electrochemical impedance characteristics of the samples and the corresponding Nyquist plots are shown in Figure 6(f). Each curve includes a semicircle in the high-frequency region and a linear par in the low-frequency region,

Table 2. Comparison of electrochemical performance with other metal compounds/biomass derived carbon composites.

Material	Biomass source	Specific capacitance	Electrolyte	Reference
Fe ₃ O ₄ /AC	macroalgae	418 F/g, 1 A/g	3 M KCl	[51]
MnO/AC	litchi shell	496.1 F/g, 1 A/g	6 M KOH	[52]
Mn ₂ O ₃ /AC	palm kernel shell	350 F/g, 1 A/g	1 M Na ₂ SO ₄	[22]
Zn-K-ATC/MnO ₂	Typha orientalis leaves	384 F/g, 1 A/g	1 M Na ₂ SO ₄	[53]
Fe ₂ O ₃ /HAC	hemp straw	256 F/g, 1 A/g	6 M KOH	[26]
α -Fe ₂ O ₃ /HPC	wheat flour	706 F/g, 1 A/g	1 M Li ₂ SO ₄	[24]
TiO ₂ @BAC	Mentha Aquatica leaves	149 F/g, 1 A/g	1 M KOH	[27]
MoS ₂ /HPGC	pomelo peel	411.4 F/g, 0.5 A/g	3 M KOH	[54]
(Ni,Co)Se-1.0/BLC	banana leaves	840.6 F/g, 1 A/g	3 M KOH	This work

with the diameter of the semicircle representing the charge transport resistance (R_{ct}) and the slope of the straight line standing for the diffusion resistance (R_w).^[49,55] It can be observed that all samples have almost overlapping semicircles in the high-frequency region, indicating that they have close R_{ct} and equivalent series resistance (R_s) which can be obtained by the intersection of the curve with the Z' axis and mainly determined by the electrolyte.^[56] In the low-frequency region, the linear slope decreases with the increase of selenide, indicating that the introduction of metal selenide will reduce the specific surface area of the material, limiting the diffusion of electrolyte ions in the composites.

The long-term cycling stability of the samples was evaluated by repeated GCD test at a current density of 2 A/g. The variation of the specific capacitance versus the cycle number is shown in Figure 6(g). Thanks to its stable porous structure, BLC1.5 has a more than 95% capacitance retention rate after 1000 charge-discharge cycles, showing the typical characteristic of EDLC. On the contrary, due to the destruction of the structure during the redox reaction, the capacitance retention rate of pure (Ni,Co)Se was only 51% after 1000 cycles. The stable carbon matrix of BLC provides some buffer space for the metal selenides.^[57] Therefore, (Ni,Co)Se-1.0/BLC exhibits a higher cycling stability of 72%. However, compared to BLC, (Ni,Co)Se-1.0/BLC sacrifices some cycling stability while increasing the specific capacitance. There may be two reasons for the capacitance attenuation of

the composite in the long-term cycling. On the one hand, the redox reaction during the charge-discharge process may cause a slight electrochemical dissolution of (Ni,Co)Se. On the other hand, the connection between the metal selenide particles and porous carbon matrix is not strong enough, some particles may fall off during the cycle, causing the decrease of specific capacitance.^[21]

The kinetic behavior of (Ni,Co)Se-1.0/BLC was explored via the cyclic voltammetry. There are two types of energy storage principles in supercapacitor: adsorption-desorption process of the electrolyte ions in the double electric layer between electrode/electrolyte interface and the rapid redox reaction on the electrode surface. Correspondingly, the charge storage is composed of surface-controlled capacitance and diffusion-controlled capacitance. Figure 7(a) shows the CV curves of (Ni,Co)Se-1.0/BLC at varying scan rates from 1 to 5 mV/s. The relationship between the peak current in CV curve and scan rate can be expressed by the following formula:^[58]

$$i = a \times v^b \quad (3)$$

where i is the peak current and v stands for scan rate. As shown in Figure 7(b), the calculated value of b is 0.8036, indicating that the composite exhibits pseudo-capacitive behavior. The proportion of the capacitance contributed by these two processes can be further calculated by the following equation:^[29,38]

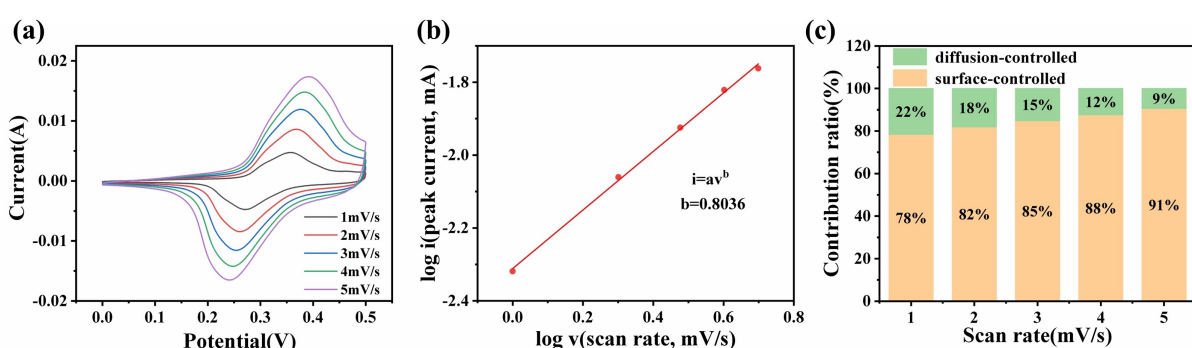


Figure 7. a) CV curves of (Ni,Co)Se-1.0/BLC at different scan rates vary from 1 to 5 mV/s. b) Charts of log (peak current) versus log (scan rate) calculated from CV curves. c) Contribution ratio of surface-controlled capacitance and diffusion-controlled capacitance at different scan rates.

$$i(V) = k_1 V + k_2 V^{1/2} \quad (4)$$

where $i(V)$, $k_1 V$ and $k_2 V^{1/2}$ represent the total current response at voltage V and the current contributed by surface-control and diffusion-control respectively. The final calculation result is shown in Figure 7(c). The contribution ratio of surface capacitance increases with the scan rate. Compared with the fast surface-controlled process, diffusion-controlled ion intercalation process is slower. With the increase of scan rate, ions have less time to react, resulting in the dominance of surface-controlled capacitance at high scan rate.

To further evaluate the application in supercapacitor of this composite, an asymmetric supercapacitor (ASC) was assembled with (Ni,Co)Se-1.0/BLC as positive electrode, BLC1.5 as negative electrode, and 3 M KOH aqueous solution as electrolyte. The CV curves of positive and negative electrode materials at 10 mV/s are shown in Fig. 8(a) where the potential windows are $-1.0\text{--}0$ V and $0\text{--}0.5$ V, respectively. Figure 8(b and c) shows the CV and GCD curves of the ASC under different potential windows, which can be extended to 1.5 V. CV curves at different scan rates ranging from 5 to 100 mV/s in Figure 8(d) further

verify the stability of the ASC at a potential window of $0\text{--}1.5$ V. The specific capacitance at different current densities can be calculated upon the GCD curves of the ASC in Figure 8(e) with the results plotted in Figure 8(f). At the current density of 1 A/g, the specific capacitance of the ASC is 109.9 F/g and remains 62 F/g when the current density increases to 10 A/g. The obvious small semicircle diameter and large linear slope in the Nyquist plot in Figure 8(g) reveal that the ASC has low charge transport resistance and diffusion resistance, exhibiting excellent electrical conductivity. Energy density and power density of the ASC are calculated in Figure 8(h) to further evaluate the energy-storage capacity. The ASC delivers a high energy density of 34.3 Wh/kg at a power density of 749.8 W/kg and the power density can reach the maximum of 7500 W/kg at the energy density of 19.4 Wh/kg, showing a better energy-storage performance than most reported supercapacitors assembled with biomass derived carbon composite, such as L-Co₃O₄(11.3 Wh/kg at 3990.6 W/kg),^[23] CuS/PPAC(25.98 Wh/kg at 2700 W/kg),^[59] CMTs-1000/Ni₂CoS₄ (28.1 Wh/kg at 753 W/kg),^[20] Mn₂O₃/AC(31 Wh/kg at 583 W/kg),^[22] TiO₂@BAC(6.96 Wh/kg at 2070 W/kg)^[27] and NBCS-Fe (17.9 Wh/kg at 400 W/kg).^[25]

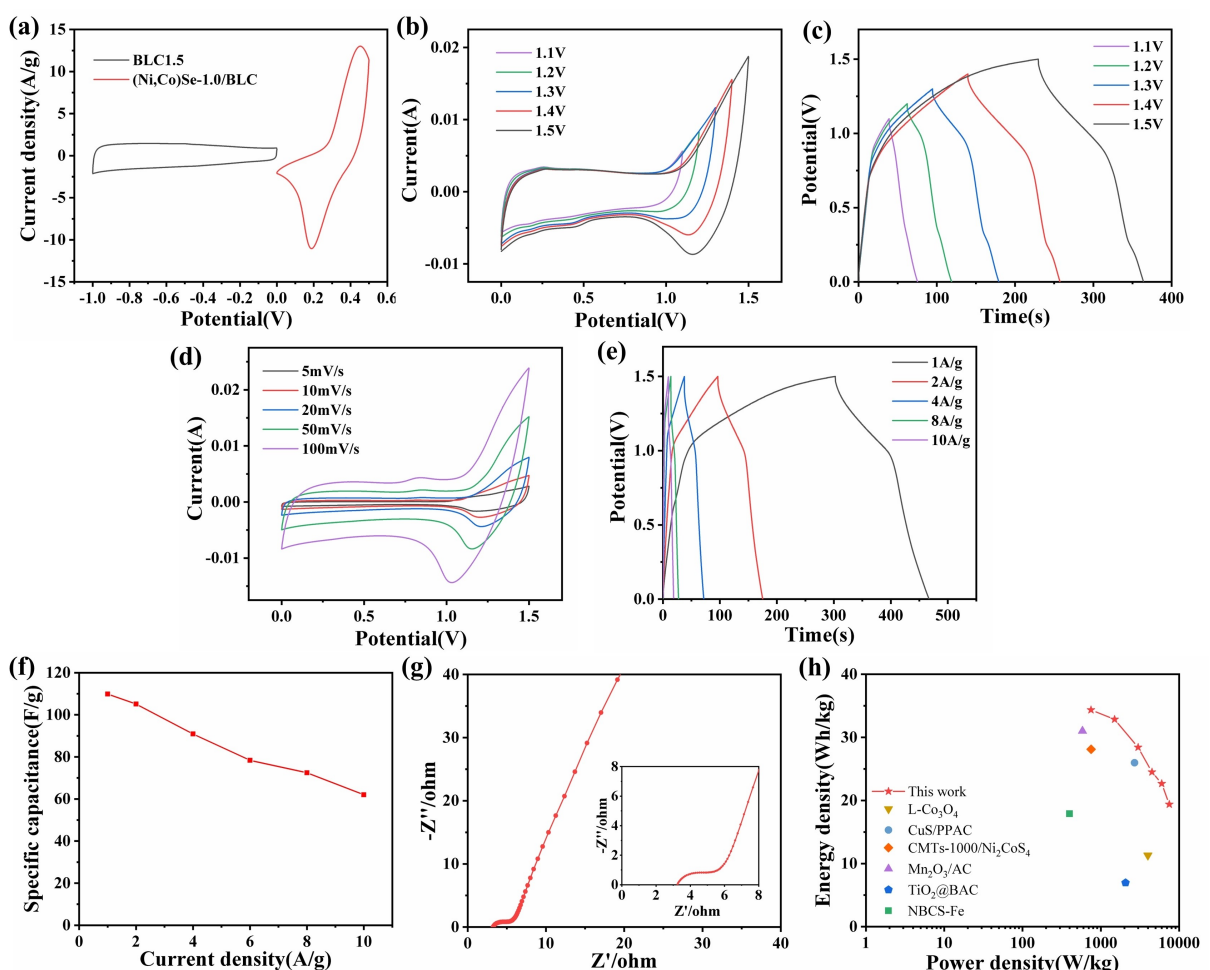


Figure 8. a) CV curves of BLC1.5 and (Ni,Co)Se-1.0/BLC at scan rate of 10 mV/s. b) CV curves of the ASC in different potential windows at 100 mV/s. c) GCD curves of the ASC in different potential windows at 1 A/g. d) CV curves of the ASC at different scan rate. e) GCD curves of the ASC at different current densities. f) specific capacitances of the ASC at different current densities. g) Nyquist plot of the ASC. h) Ragone plot of the ASC.

Conclusions

In this work, banana leaves derived carbon was prepared by two-step carbonization with KOH as activator. When the ratio of BL to KOH is 1:1.5, the prepared biomass derived carbon has a specific surface area of $1068 \text{ m}^2/\text{g}$ and exhibits the highest specific capacitance among all the prepared samples. (Ni,Co)Se/BLC composites with different loads of metal selenide were successfully prepared by the following hydrothermal process. The composites retain the hierarchical porous interconnected structure of BLC and the selenide particles are evenly distributed. Since the biomass derived carbon matrix provides adequate channel for fast ion transport and effectively prevents the agglomeration of the selenide particles, (Ni,Co)Se-1.0/BLC exhibits a specific capacitance of 840.6 F/g , which is much higher than that of pure BLC and (Ni,Co)Se. The assembled high-performance asymmetric supercapacitor with high energy density (34.3 Wh/kg) and power density (7500 W/kg) further verifies the application of the prepared materials in supercapacitor. Taken together, appropriate metal selenide loading can greatly improve the electrochemical performance of biomass derived carbon, thus enhancing their application potential in supercapacitor electrodes.

Experimental Section

Materials

Banana leaves were collected from the plantations in southern China. All the chemicals used in this work were analytical reagent (AR) grade. Potassium hydroxide (KOH) was from Macklin Co. Ltd. Nickel acetate tetrahydrate ($\text{Ni}(\text{CH}_3\text{COO})_2 \cdot 4\text{H}_2\text{O}$) was purchased from Tianjin Damao Co., Ltd. Cobalt nitrate hexahydrate ($\text{Co}(\text{CH}_3\text{COO})_2 \cdot 4\text{H}_2\text{O}$) and selenium dioxide (SeO_2) were supplied by Aladdin Reagent Co., Ltd.

Preparation of BLC and (Ni,Co)Se/BLC composite

After washing and drying, the banana leaves were pre-carbonization at 250°C for 3 h to remove the inorganic impurities. Then the leaves were ground into powder and added to 1 M KOH aqueous solution with a powder/alkali mass ratio of 1:1, 1:1.5, 1:2 and 1:2.5, mixing at room temperature for 3 h. The mixtures were evaporated to dry at 80°C , then transferred into tube furnace at 700°C for 3 h under argon flow. The products were washed with 0.5 M HCl followed by deionized water until the filtrate became neutral and labeled as BLC n , where n indicates the alkali-carbon ratio.

The (Ni,Co)Se/BLC composite was synthesized using one-step hydrothermal method. In a typical procedure, $\text{Ni}(\text{CH}_3\text{COO})_2 \cdot 4\text{H}_2\text{O}$, $\text{Co}(\text{CH}_3\text{COO})_2 \cdot 4\text{H}_2\text{O}$ and SeO_2 were dissolved into 70 ml benzyl alcohol in a molar ratio of 1:1:2. As shown in Table S1. The specific amounts of SeO_2 in different contrast samples were 0.5, 0.75, 1, 1.5 mmol, respectively. Then, 0.12 g of BLC1.5 was added into the mixed solution above followed by ultrasonic treatment for 20 min, stirring for 1 h to disperse the carbon evenly. The mixture was transferred into a 100 ml Teflon-lined hydrothermal reactor and heated to 180°C for 15 h. After natural cooling to room temperature, (Ni,Co)Se/BLC composite was obtained by final centrifugation, washed with ethanol and dried at 60°C overnight. The

products were donated as (Ni,Co)Se- n /BLC, where n stands for the amount of SeO_2 . For comparison, pure (Ni,Co)Se is also synthesized in the same way without adding BLC1.5.

Material characterization

The crystal structures of samples were measured by X-ray diffraction system with Cu K α irradiation (XRD; PANalytical, X'PertPRO, $\lambda=0.15418 \text{ nm}$) and Raman spectrometer (Horiba Jobin Yvon, HJY LabRAM Aramis). The morphology and structure were characterized via field-emission scanning electron microscopy (SEM; FEI, Novanano430) and transmission electron microscopy (TEM; JEOL, JEM 2100F) equipped with an energy dispersive X-ray detector (EDX). The chemical composition was investigated using X-ray photoelectron spectroscopy (XPS; ThermoFisher, ESCALAB Xi +). And the specific surface area and pore size distribution were determined via the Brunauer–Emmett–Teller (BET) methods with Micromeritics ASAP 2020.

Electrochemical measurements

The electrochemical properties of samples were tested on electrochemical workstation (CHI660D, Shanghai Chenhua Co., Ltd.) with a three-electrode configuration in 3 M KOH electrolyte, where a piece of platinum foam was employed as the counter electrode, and Hg/HgO electrode as the reference electrode. The working electrode was prepared using drop-drying strategy with a nickel foam (1 cm \times 1 cm) as substrate which had been washed with 0.5 M HCl, deionized water and ethanol. The sample, polytetrafluoroethylene (PTFE) and carbon black with a mass ratio of 8:1:1 were dispersed into anhydrous ethanol and ground in an agate mortar to attain a slurry, which was then coated on the Ni foam, and pressed at 10 MPa. The electrochemical performance of the sample was tested by cyclic voltammetry (CV), galvanostatic charge and discharge (GCD) and electrochemical impedance spectroscopy (EIS). The specific capacitance of the sample was calculated through GCD curves according to the following equation:^[49,60]

$$C = \frac{I \times \Delta t}{m \times \Delta V} \quad (5)$$

where C is the specific capacitance of the electrode (F/g), I represents the discharge current (A), Δt refers to the discharge time (s), m is the mass of the active materials (g) and ΔV is the potential window (V).

For the two-electrode test, the asymmetric supercapacitor was assembled using the CR2032 coin cell with (Ni,Co)Se/BLC composite as the positive electrode, BLC as the negative electrode and polypropylene non-woven fabric as the diaphragm. The relationship between the mass of active substances in the two electrodes was revealed by the equation:^[37,61]

$$\frac{m_+}{m_-} = \frac{C_- \Delta V_-}{C_+ \Delta V_+} \quad (6)$$

where m_+ , m_- , C_+ , C_- , ΔV_+ , ΔV_- are the mass of active substances (g), specific capacitance values (F/g), discharge voltage (V) of positive and negative electrodes, respectively.

The specific capacitance (C_{cell} , F/g), energy density (E , Wh/kg) and power density (P , W/kg) of the asymmetric supercapacitor were calculated by the subsequent equations:^[20]

$$C_{\text{cell}} = \frac{I \times \Delta t}{m_t \times \Delta V} \quad (7)$$

$$E = \frac{c_{\text{cell}} \times \Delta V^2}{2 \times 3.6} \quad (8)$$

$$P = \frac{3600E}{\Delta t} \quad (9)$$

where m_t is the total mass of the active substances in the two electrodes (g).

Acknowledgements

This work is financially supported by National Natural Science Foundation of China (Grant No. 51873074).

Conflict of Interests

The authors declare no conflict of interest.

Data Availability Statement

The data that support the findings of this study are available from the corresponding author upon reasonable request.

Keywords: biomass derived carbon • composite • energy storage • Ni–Co selenide • supercapacitor

- [1] X. P. Li, J. U. Zhang, B. Liu, Z. P. Su, J. J. Klemes, *J. Cleaner Prod.* **2021**, *310*, 127428.
- [2] B. K. Roy, I. Tahmid, T. U. Rashid, *J. Mater. Chem. A* **2021**, *9*, 17592–17642.
- [3] P. Manasa, S. Sambasivam, F. Ran, *J. Energy Storage* **2022**, *54*, 105290.
- [4] J. G. Ruiz-Montoya, L. V. Quispe-Garrido, J. C. C. Gomez, A. M. Baena-Moncada, J. M. Goncalves, *Sustain. Energy Fuels* **2021**, *5*, 5332–5365.
- [5] X. F. Tang, D. Liu, Y. J. Wang, L. F. Cui, A. Ignaszak, Y. Yu, J. J. Zhang, *Prog. Mater. Sci.* **2021**, *118*, 100770.
- [6] H. Liu, X. Cai, X. J. Zhi, S. L. Di, B. Y. Zhai, H. G. Li, S. L. Wang, L. Li, *Nano-Micro Lett.* **2023**, *15*, 24.
- [7] S. Wu, X. Yan, X. Sun, S. Tian, J. Wang, C. Liu, S. Sun, L. Wu, X. Zhao, Q. Yang, *J. Energy Storage* **2023**, *71*, 108152.
- [8] P. Chen, Y. Tang, Y. Gao, Y. Zhang, L. Liu, *J. Power Sources* **2023**, *580*, 233334.
- [9] S. Sundriyal, V. Shrivastav, H. D. Pham, S. Mishra, A. Deep, D. P. Dubal, *Resour. Conserv. Recycl.* **2021**, *169*, 105548.
- [10] T. Cen, L. Chen, X. J. Zhang, Y. H. Tian, X. X. Fan, *Electrochim. Acta* **2021**, *367*, 137488.
- [11] C. J. Zhao, J. J. Guo, J. T. Fan, X. Zhang, C. H. Zhao, S. Chen, *J. Energy Storage* **2022**, *46*, 103786.
- [12] A. H. Khadem, T. Ul Hasan, A. Rahman, S. A. Smriti, S. Alimuzzaman, *J. Energy Storage* **2022**, *56*, 105988.
- [13] S. K. Babu, M. Jayachandran, T. Maiyalagan, T. Vijayakumar, B. Gunasekaran, *Mater. Lett.* **2021**, *302*, 130338.
- [14] C. J. Zhao, Y. Z. Ding, Z. Q. Zhu, S. F. Han, C. H. Zhao, G. R. Chen, *Nanotechnology* **2021**, *32*, 395606.
- [15] S. Saini, P. Chand, A. Joshi, *J. Energy Storage* **2021**, *39*, 102646.
- [16] S. Yang, S. L. Wang, X. Liu, L. Li, *Carbon* **2019**, *147*, 540–549.
- [17] G. S. Jiang, R. A. Senthil, Y. Z. Sun, T. R. Kumar, J. Q. Pan, *J. Power Sources* **2022**, *520*, 230886.
- [18] C. K. Roy, S. S. Shah, A. H. Reaz, S. Sultana, A. Chowdhury, S. H. Firoz, M. H. Zahir, M. A. A. Qasem, M. A. Aziz, *Chemistry-an Asian Journal* **2021**, *16*, 296–308.
- [19] A. Apriwandi, E. Taer, R. Farma, R. N. Setiadi, E. Amiruddin, *J. Energy Storage* **2021**, *40*, 102823.
- [20] K. Wang, R. Yan, X. D. Tian, Y. Wang, S. W. Lei, X. Li, T. Yang, X. J. Wang, Y. Song, Y. Q. Liu, Z. J. Liu, Q. G. Guo, *Electrochim. Acta* **2019**, *302*, 78–91.
- [21] C. J. Yuan, H. B. Lin, H. Y. Lu, E. D. Xing, Y. S. Zhang, B. Y. Xie, *Appl. Energy* **2016**, *178*, 260–268.
- [22] B. L. Vijayan, G. M. Misnon, II, A. Kumar, K. Miyajima, M. V. Reddy, K. Zaghib, C. Karuppiyah, C. C. Yang, R. Jose, *J. Colloid Interface Sci.* **2020**, *562*, 567–577.
- [23] X. B. Xie, C. X. Hou, D. Wu, X. Q. Sun, X. Y. Yang, Y. P. Zhang, R. H. Yu, S. Z. Zhang, H. Kimura, W. Du, *J. Alloys Compd.* **2022**, *891*, 161967.
- [24] P. P. Yu, W. Duan, Y. F. Jiang, *Front. Chem.* **2020**, *8*, 611852.
- [25] P. Y. Li, H. Y. Xie, X. Q. Wang, Y. Xie, Y. B. Wang, Y. K. Zhang, *Sustain. Energy Fuels* **2020**, *4*, 4522–4530.
- [26] X. Jiang, G. F. Shi, G. Y. Wang, P. Mishra, J. W. Du, Y. Zhang, *Ionics* **2020**, *26*, 4039–4051.
- [27] A. A. Ahmed, C. Bathula, R. Soni, H. S. Kim, H. Im, S. W. Lee, W. K. Kim, S. Gedi, A. N. Kadam, *Chemosphere* **2022**, *289*, 133197.
- [28] H. Liu, X. Liu, S. L. Wang, H. K. Liu, L. Li, *Energy Storage Mater.* **2020**, *28*, 122–145.
- [29] Q. F. Wang, X. Ran, W. K. Shao, M. H. Miao, D. H. Zhang, *J. Power Sources* **2021**, *490*, 229517.
- [30] S. Manickam, H. Kuzhandaivel, Y. Selvaraj, M. C. Franklin, K. S. Nallathambi, *Dalton Trans.* **2022**, *51*, 1542–1552.
- [31] J. Liu, L. X. Ren, J. J. Luo, T. T. Zhang, *J. Solid State Electrochem.* **2022**, *26*, 2861–2871.
- [32] L. Sun, Y. Liu, B. F. Luo, F. R. Yan, X. Y. Liu, F. F. Zhu, W. D. Shi, *Chem. Eng. J.* **2023**, *454*, 140088.
- [33] L. C. Zhao, P. Zhang, Y. N. Zhang, Z. Zhang, L. Yang, Z. G. Chen, *J. Mater. Sci. Technol.* **2020**, *54*, 69–76.
- [34] M. S. U. Shah, X. Q. Zuo, A. Shah, S. I. Al-Saeedi, M. Z. U. Shah, E. A. Alabbad, H. Y. Hou, S. A. Ahmad, M. Arif, M. Sajjad, T. Ul Haq, *J. Energy Storage* **2023**, *65*, 107267.
- [35] H. Chen, W. L. Li, M. He, X. W. Chang, X. L. Zheng, Z. Y. Ren, *J. Alloys Compd.* **2021**, *855*, 157506.
- [36] J. Y. Wang, S. Sarwar, J. Song, L. J. Du, T. B. Li, Y. D. Zhang, B. B. Li, Q. P. Guo, J. J. Luo, X. Y. Zhang, *J. Alloys Compd.* **2022**, *892*, 162079.
- [37] H. C. Chen, M. Q. Fan, C. Li, G. L. Tian, C. J. Lv, D. Chen, K. Y. Shu, J. J. Jiang, *J. Power Sources* **2016**, *329*, 314–322.
- [38] Y. Z. Liu, P. H. Liu, L. Li, S. H. Wang, Z. L. Pan, C. W. Song, T. H. Wang, *J. Electroanal. Chem.* **2021**, *903*, 115828.
- [39] W. B. Zhang, B. Liu, M. Yang, Y. J. Liu, H. M. Li, P. L. Liu, *J. Mater. Sci. Technol.* **2021**, *95*, 105–113.
- [40] W. J. Lu, X. H. Cao, L. N. Hao, Y. P. Zhou, Y. W. Wang, *Mater. Lett.* **2020**, *264*, 127339.
- [41] S. Y. Yao, Z. H. Zhang, Y. M. Wang, Z. Liu, Z. Li, *J. Energy Storage* **2021**, *44*, 103259.
- [42] H. B. Pei, G. L. Liu, R. B. Guo, N. J. Liu, Z. L. Mo, *Int. J. Hydrogen Energy* **2022**, *47*, 35227–35240.
- [43] M. Zhu, Y. D. Yan, Q. Yan, J. L. Yin, K. Cheng, K. Ye, K. Zhu, J. Yan, D. X. Cao, G. L. Wang, *Int. J. Hydrogen Energy* **2020**, *45*, 10486–10493.
- [44] B. Yu, Y. Hu, F. Qi, X. Q. Wang, B. J. Zheng, K. Liu, W. L. Zhang, Y. R. Li, Y. F. Chen, *Electrochim. Acta* **2017**, *242*, 25–30.
- [45] L. R. Hou, X. Sun, L. Z. Guo, X. T. Meng, J. X. Wei, C. Z. Yuan, *Energy Technol.* **2020**, *8*, 1901319.
- [46] L. Tian, Z. Y. Chen, T. J. Wang, M. Cao, X. H. Lu, W. J. Cheng, C. C. He, J. Wang, Z. Li, *Nanoscale* **2022**, *15*, 259–265.
- [47] X. Li, H. J. Wu, C. Guan, A. M. Elshahawy, Y. T. Dong, S. J. Pennycook, J. Wang, *Small* **2019**, *15*, 1803895.
- [48] J. J. Han, Q. Li, C. Peng, N. Shu, F. Pan, J. Q. Wang, Y. W. Zhu, *Appl. Surf. Sci.* **2020**, *502*, 144191.
- [49] C. J. Verma, A. Kumar, S. Pal, S. Sinha, A. K. Singh, A. Jaiswal, R. Prakash, *Renewable Energy* **2020**, *162*, 2285–2296.
- [50] S. Sundriyal, V. Shrivastav, A. Kaur, Mansi, A. Deep, S. R. Dhakate, *Journal of Energy Storage* **2021**, *41*, 103000.
- [51] S. E. M. Pourhosseini, O. Norouzi, P. Salimi, H. R. Naderi, *ACS Sustainable Chem. Eng.* **2018**, *6*, 4746–4758.
- [52] N. Zhao, L. B. Deng, D. W. Luo, P. X. Zhang, *Appl. Surf. Sci.* **2020**, *526*, 146696.
- [53] T. T. Yu, F. M. Wang, X. B. Zhang, G. J. Lv, H. H. Lv, J. W. Wang, Y. Zhai, M. Z. Li, *Diamond Relat. Mater.* **2021**, *116*, 108450.
- [54] Q. J. Lin, J. M. Wang, J. H. Chen, Q. Yang, L. J. Fang, Y. D. Huang, *J. Electrochim. Soc.* **2022**, *169*, 020502.
- [55] C.-M. Yoon, S. Jekal, D.-H. Kim, J. Noh, J. Kim, H.-Y. Kim, C.-G. Kim, Y.-R. Chu, W.-C. Oh, *Nanomaterials* **2023**, *13*, 1614.

- [56] P. M. Anjana, J. F. J. Sherin, C. Vijayakumar, S. R. S. Kumar, M. R. Bindhu, R. B. Rakhi, *Mater. Sci. Eng. B* **2023**, 290, 116313.
- [57] F. Z. Zhang, P. C. Sherrell, W. Luo, J. Chen, W. Li, J. P. Yang, M. F. Zhu, *Adv. Sci.* **2021**, 8, 2102859.
- [58] D. Khalafallah, X. Y. Li, M. J. Zhi, Z. L. Hong, *ACS Appl. Nano Mater.* **2021**, 4, 14258–14273.
- [59] C. X. Li, P. He, L. P. Jia, X. Q. Zhang, T. H. Zhang, F. Q. Dong, M. Q. He, S. Wang, L. H. Zhou, T. T. Yang, H. H. Liu, *Electrochim. Acta* **2019**, 299, 253–261.
- [60] Z. H. Xu, X. M. Zhang, Y. Liang, H. J. Lin, S. Zhang, J. L. Liu, C. D. Jin, U. Choe, K. C. Sheng, *Energy Fuels* **2020**, 34, 8966–8976.
- [61] X. Y. Huang, Y. Yang, J. L. Zhao, Y. Huang, X. H. Wang, *J. Alloys Compd.* **2023**, 947, 115828.

Manuscript received: August 19, 2023

Revised manuscript received: September 6, 2023

Accepted manuscript online: September 11, 2023

Version of record online: September 21, 2023